

Engineering Solution-Processed Non-Crystalline Solid Electrolytes for Li Metal Batteries

Pooja Vadhva,^a Thomas E. Gill,^a Joshua H. Cruddos,^{a,b} Samia Said,^a Marco Siniscalchi,^c Sudarshan Narayanan,^{b,c} Mauro Pasta,^{b,c} Thomas S. Miller,^{a,c} Alexander J. E. Rettie^{a,c,*}

^a Electrochemical Innovation Lab, Department of Chemical Engineering, University College London, WC1E 6DH (UK)

^b The Faraday Institution Quad One, Harwell Science and Innovation Campus, Didcot OX11 0RA (UK)

^c Department of Materials, University of Oxford, OX1 3PH (UK)

* For correspondence: a.rettie@ucl.ac.uk

Keywords: solid-state battery, non-crystalline, solid electrolyte, thin film, scalable, ionic conductivity

ABSTRACT: Non-crystalline Li⁺-ion solid electrolytes (SEs), such as lithium phosphorous oxynitride, can uniquely enable high-rate solid-state battery operation over thousands of cycles in thin film form. However, they are typically produced by expensive and low throughput vacuum deposition, limiting their wide application and study. Here, we report a non-crystalline SE of composition Li-Al-P-O (LAPO) with an ionic conductivity $>10^{-7}$ S cm⁻¹ at room temperature by spin coating from aqueous solutions and subsequent annealing in air. Homogenous, dense, flat layers can be synthesised with sub-micron thickness at temperatures as low as 230 °C. Control of the composition is shown to significantly affect the ionic conductivity, with increased Li and decreased P content being optimal, while higher annealing temperatures result in decreased ionic conductivity. Activation energy analysis reveals a Li⁺-ion hopping barrier of 0.42(1) eV. Additionally, these SEs exhibit low room temperature electronic conductivity ($<10^{-11}$ S cm⁻¹) and moderate Young's modulus of ≈ 54 GPa, which may be beneficial in preventing Li dendrite formation. In contact with Li metal, LAPO is found to form a stable, but high impedance passivation layer comprised of Al metal, Li-P and Li-O species. These findings should be of value when engineering non-crystalline SEs for Li-metal batteries with high energy and power densities.

1. INTRODUCTION

Over the past few decades, lithium-ion battery (LIB) technology has enabled a wide range of applications, principally: portable electronic devices, wearable devices, electric vehicles, and grid storage.^{1,2} However, with LIBs reaching maturity, a new generation of advanced batteries with increased energy and power densities are needed to usher in sweeping decarbonisation and meet ambitious climate targets. Lithium metal anodes offer a $\approx 10\times$ theoretical energy density compared to graphite anodes used in LIBs,^{3,4} but the use of traditional liquid electrolytes results in short cycle life as well as safety concerns due to dendrite formation in the presence of flammable solvents. Solid electrolytes (SEs) have been proposed to block dendrite propagation due to their stiffness and high transference number.^{5,6} Recently, crystalline SEs with ionic conductivity (σ_{ion}) values rivaling liquid electrolytes have been discovered⁷ but despite their solid form, all suffer from Li dendrite propagation at practical (dis)charge rates. In addition, unstable interphase formation and difficulty of manufacturing at scale are outstanding challenges.^{4–6,8–11}

Non-crystalline SEs may uniquely meet these stringent requirements.^{11–16} One such material, lithium phosphorus

oxynitride (LiPON) has demonstrated a long cycle life and high-rate operation^{17–20} in a thin-film solid-state battery (SSB). These properties have motivated work to understand its low impedance interphase and resistance to dendrite formation. Cryo-transmission electron microscopy showed that the interphase consisted of nanoscale domains of Li₂O, Li₃P and Li₃PO₄ in an amorphous LiPON matrix ≈ 100 nm thick,²¹ although electrochemical techniques suggested an interphase thickness of 5 nm.²² This stable interphase has enabled its use as a Li-anode protection coating in Li-ion, Li-sulfur and Li-air cells.^{23–25} Regarding dendrite formation, the amorphous nature of LiPON minimises surface roughness and grain boundaries in the bulk which may act as sites for dendrite nucleation and growth.²⁶ Recent work has also suggested that LiPON's low electronic conductivity (σ_e) may be an important aspect in its ability to block dendrites.¹⁴ However, applicability of LiPON at scale is limited as it is produced by costly and low throughput vacuum deposition techniques.

New non-crystalline SEs produced by scalable methods would be of great interest for advanced batteries.¹² Solution-based processing involving direct deposition of precursor solutions followed by a moderate temperature annealing step can function as a low energy alternative to the conventional high temperature routes used for ceramic

SEs.^{27,28} There have been several reports of non-crystalline SE fabrication using organic solvents in moisture-free conditions^{29–31}, but production in air using water as a solvent would be most desirable for low cost and sustainable manufacturing. Extremely smooth, dense amorphous films from aqueous solutions have long been of interest for microelectronic applications³² and this framework was recently extended to Li-containing materials by Clayton et al.³³ Although dense, smooth films were achieved, the σ_{ion} of these films was too low for solid electrolyte applications ($\approx 10^{-8}$ S cm⁻¹ vs. $\approx 10^{-6}$ S cm⁻¹ for LiPON).³⁴

Here, we report non-crystalline Li-Al-P-O (LAPO) phases with desirable SE properties synthesised from solution. First, we rationally explore this phase space and find thin film materials with $\sigma_{\text{ion}} > 10^{-7}$ S cm⁻¹. Then, the effects of annealing temperature on the σ_{ion} , film structure, surface roughness and chemical composition are studied. The optimised SE is shown to exhibit a small barrier to Li⁺-ion transport, low σ_{e} , and mechanical properties comparable to LiPON. Finally, the electrochemical stability against Li-metal is probed and the chemical composition of the resultant interphase determined.

2. EXPERIMENTAL METHODS

2.1 Film fabrication

Li-Al-P-O thin films were synthesised by spin coating from aqueous precursor solutions, followed by an annealing step in air as described previously.³³ In a typical synthesis, 50 mmol of Al(NO₃)₃•9H₂O (Sigma Aldrich) was added to 50 mL of de-ionised (DI) water and stirred for 1 hr until completely dissolved. To this solution, 63 mmol of H₃PO₄ (85% concentrated in water) was added and stirred overnight at 80 °C. After cooling to room temperature, 137.5 mmol of LiNO₃ (Fisher Scientific) was added. Finally, the solution was diluted with DI water to achieve a final concentration of 0.4 M with respect to Al. This final concentration was used for all precursor solutions with the moles of LiNO₃ or H₃PO₄ being varied to achieve a range of Li:Al:P ratios during compositional exploration.

Silicon (Si) substrates (p-type, boron-doped, single-side polished, resistivity <0.1 cm, PI-KEM), were used as electrically conductive back contacts with low roughness. These were cut into 2×2 cm² squares using a diamond scribe and sonicated separately in acetone and then IPA for 5 min, rinsing with DI water in between. Subsequently, the substrates were dried using a N₂ gun before being O₂ plasma-treated (Henniker HPT-100) at 100 W for 5 min to produce a hydrophilic surface.

The precursor solution was sonicated at 40 °C for 1 h and cooled to room temperature before being twice filtered using a 0.2 µm Teflon filter attached to a syringe. The solution was flooded onto the substrate, spin coated at 3000 rpm for 30 s (after a ramp rate of 6000 rpm s⁻¹) and immediately transferred to a pre-heated hot plate at 275 °C for 1 min. The process was repeated for multi-layer films, by allowing the film to cool to room temperature before spin coating the next layer. After the designated

number of layers were deposited, a final anneal at the desired temperature was carried out for 1 h. For the films annealed above 275 °C, a box furnace was used with a 5 °C min⁻¹ ramp rate. For the films annealed at 230 °C, the pre-heated hot plate was set at 230 °C so that the films were not exposed to a temperature above this value. Unless otherwise stated, the film annealing temperature was 275 °C as this was found to produce films with high σ_{ion} and low surface roughness.

2.2 Physical characterisation

Film thickness was determined using a LEO Gemini 1525 field emission scanning electron microscope (SEM). For cross-sectional imaging the brittle-fracture method was used, and a thin Au layer was sputtered to minimise charging. Multi-layer films were used for ease of imaging. The film morphology and mechanical properties were characterised using atomic force microscopy (AFM, Bruker Dimension Icon with ScanAsyst) across a 10×10 µm² film area with the average roughness calculated from 3 different areas across 1×1 µm² using the PeakForce Quantitative Nanoscale Mechanical mode. The PeakForce tapping mode was adopted in all cases with an RTESPA-525 Si probe with reflective Al coating (Bruker Corp., k = 200 N m⁻¹, f₀ = 525 kHz). For mechanical property measurements, the probe was calibrated by the relative method, using highly oriented pyrolytic graphite (HOPG) with a nominal elastic modulus of 18 GPa for reference. At each point in the scan, alongside the morphology, the probe performed nanoindentation measurements and recorded the load and displacement of the specialised tips and cantilevers to produce a load-displacement curve. This curve was used to calculate the elastic modulus of the materials, by fitting to the DMT (Derjagin, Muller, Toropov) model.³⁵ All of the results obtained by the AFM were analysed by Nanoscope Analysis software.

2.3 Chemical characterisation

The film composition was determined using X-ray photoelectron spectroscopy (ThermoFisher, K-alpha XPS system, Al source) with binding energies referenced against the adventitious carbon 1s peak at 284.4 eV. A survey scan and regions around elements of interest were conducted. For lighter elements such as Li, a minimum of 30 scans were acquired.

In situ XPS coupled with Li sputtering was conducted in an in-house set-up, using a Phi XPS VersaProbe III with an Al Kα X-ray source generating focused, monochromatic Al Kα X-rays at 1486.6 eV under ultrahigh vacuum conditions with the main chamber maintained at pressures between 10⁻⁷ and 10⁻⁶ Pa. Here, Li metal (3×3mm², 750 µm thick, Sigma Aldrich) was attached to a sample holder within the XPS chamber, similar to the setup described by Wenzel et al. previously.³⁶ The LAPO sample and Li metal were transferred to the XPS chamber using a vacuum transfer vessel directly from a glovebox to minimise air exposure. Li sputtering was conducted using an Ar⁺ ion gun, at an acceleration voltage of 4 kV and beam current of 2.8 µA with data

were collected at intervals of 5 min. CasaXPS software was used to analyse the XPS data and quantify the chemical composition using Shirley background fitting. The spectra obtained prior to lithium deposition were charge corrected to adventitious C at 284.8 eV through acquired C 1s spectra. After lithium deposition the Li₂O peak at 528.5 eV in the O 1s spectra was used for charge-correction.

Grazing incidence X-ray diffraction (GI-XRD) was performed on a Bruker D8 Discover diffractometer with a microfocus Cu source and Vantec 500 2D detector. These films were spin coated onto fused silica substrates to reduce scattering from the substrate. The fused silica substrates were cleaned using the same procedure as the Si wafers and were purchased pre-cut to 2×2 cm², with a thickness of 1 mm from Multi-lab. The scans were performed in a theta-theta geometry with 4 frames at 120 s per frame and the sample was rotated in the beam during collection.

2.4 Electronic and electrochemical characterisation

Through-plane ionic conductivity measurements were performed to make a realistic comparison of the Li⁺-ions moving through the SE film during cell cycling. Circular Au top contact pads (1.2 mm diameter, ≈80 nm thickness) were deposited by sputtering through a shadow mask. For the bottom contact, Al foil was attached to the back of the Si substrate using conductive epoxy (Agar Scientific). An in-house cell holder was designed to take conductivity measurements, where an Au-plated screw with a rounded tip gently contacted the Au pads. In all cases 4-layer films were used as thinner films could be damaged by the screw contact pressure. The Au screw and Al back contact were connected to a potentiostat (Reference 600+, Gamry) for electrochemical measurements. Electrochemical impedance spectroscopy (EIS) was conducted using a 5 mV perturbation voltage over a frequency range of 50 Hz to 1 MHz. The EIS data were fit using an equivalent circuit model (ECM) consisting of elementary components in a Randles type circuit.^{37,38} A resistor (R) and constant phase element (CPE) in parallel were used to model different relaxation processes, where R_o accounts for the impedance due to the ohmic resistance from electrical contacts, R_l is assigned to the bulk SE impedance (R_b) of LAPO and the CPE_w accounted for the electrode polarization due to the non-symmetric blocking electrodes.³⁹

The ionic conductivity, σ_{ion} was calculated using Equation 1:

$$\sigma_{ion} = \frac{l}{RA} \quad (1)$$

where, l is the thickness of the film, R is the bulk SE resistance and A is the geometric area. The value was averaged from 3 different films, with each film being sampled in multiple positions (>3) across the film.

The temperature dependence of the σ_{ion} was fit to an Arrhenius relationship:^{40,41}

$$\sigma_{ion}(T) = \sigma_0(T) e^{-E_a/kT} \quad (2)$$

where, $\sigma_0(T)$ is a pre-exponential factor dependent on temperature, E_a is the activation energy, k is the Boltzmann constant and T is temperature.

For the DC polarisation experiments, a voltage bias of 1 V was applied for 1 h and the current-voltage curve fit to an exponential decay function. A longer duration constant-voltage experiment was run over 12 h, which confirmed that 1 h was sufficient to reach steady state.

Finally, the electrochemical stability of LAPO with Li metal was probed by thermally evaporating Li (MBraun, EVAP) to form circular contacts (1 mm diameter, 1 μ m thickness) onto a LAPO film on a Si substrate which had been dried in a Buchi oven at 60 °C overnight. Cu was used as the current collector and the cell was sealed under Ar in a pouch cell bag. The cell was clamped between two plates to ensure good electrical connection. EIS was conducted at room temperature over 13 h with a Biologic MTZ-35 potentiostat, between 1 Hz and 3.7 MHz. To separate polarisation contributions from the various cell components and identify all time processes in the system, a Fourier transform of the EIS data was performed for distribution of relaxation times (DRT) analysis by,^{42,43}

$$Z(w) = R_{ohmic} + Z_{pol}(w) \\ = R_{ohmic} + \sum_{i=1}^N \frac{R_{pol,k}}{1 + j\omega\tau_k} \quad (3)$$

where R_{ohmic} is the Ohmic resistance of the SSB and is independent of frequency, while $Z_{pol}(w)$ accounts for the polarisation resistance, $R_{pol,k}$ and is a function of frequency. This deconvolution is possible since the different cell processes have characteristic frequencies, and therefore time constants, associated with specific processes (Table 2). A MATLAB code by Wan et al.⁴³ was used to perform DRT analysis. The Li deposition and cell assembly were carried out in an Ar-filled glovebox (MBraun, <1 ppm H₂O and O₂).

3. RESULTS AND DISCUSSION

3.1 Compositional engineering

Previous work³³ determined a room temperature σ_{ion} value of 2.6×10^{-8} S cm⁻¹ for the single composition Li_{2.5}Al₁P_{1.5}O_{5.5} (based on the bulk glass 0.5Li₂O-0.2Al₂O₃-0.3P₂O₅)⁴⁴ annealed at 275 °C. Because elemental composition can strongly affect the conduction properties of SEs,^{44,45} we systematically adjusted the Li and P ratios relative to Al in Li_aAl₁P_cO_x whilst keeping the annealing temperature constant at 275 °C. Note that a values were de-

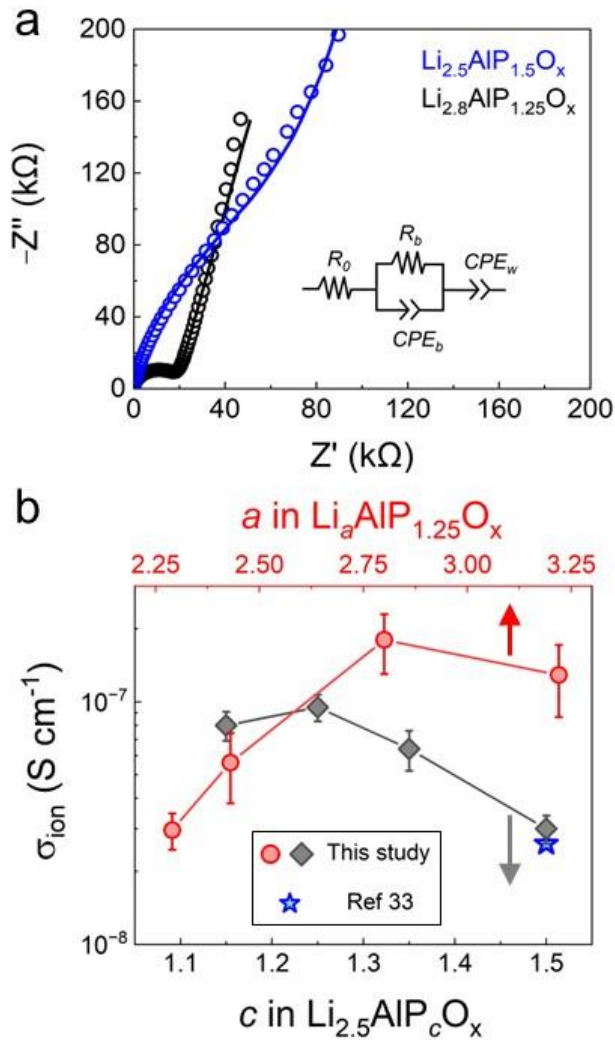


Figure 1. a) EIS Nyquist plots for two LAPO compositions with the equivalent circuit model used to fit the data (inset). b) σ_{ion} for various LAPO compositions determined from the fitted EIS data.

terminated by XPS, while c represents the nominal amount of phosphorous in the precursor solutions. First, the P content in $\text{Li}_{2.5}\text{Al}_1\text{P}_c\text{O}_x$ was varied in the range $1.1 < c < 1.5$ (Figure 1). Note the good agreement with the previous work of Clayton et al., at $c = 1.5$. As the P content was decreased from 1.5 to 1.25, an increase in σ_{ion} from $3.0(4) \times 10^{-8} \text{ S cm}^{-1}$ to $0.95(12) \times 10^{-7} \text{ S cm}^{-1}$ was observed. Values of c below 1.15 resulted in films with poor coverage. Fixing the optimal value of $c = 1.25$, the Li content (a value) was subsequently varied. By increasing a from 2.25 to 2.8, the σ_{ion} increased by almost an order of magnitude (from $3.0(5) \times 10^{-8} \text{ S cm}^{-1}$ to $1.8(5) \times 10^{-7} \text{ S cm}^{-1}$) highlighting the sensitivity of σ_{ion} to both Li and P content. Finally, the effect of P content in the Li-rich $\text{Li}_{2.8}\text{Al}_1\text{P}_c\text{O}_x$ was investigated, which confirmed the same optimal composition (see Figure S1 in the Supporting Information (SI)). Therefore, our initial exploration of the Li-Al-P-O phase space yielded a maximum σ_{ion} of $1.8(5) \times 10^{-7} \text{ S cm}^{-1}$ for the composition

$\text{Li}_{2.8}\text{Al}_1\text{P}_{1.25}\text{O}_x$. To the best of our knowledge, this is the highest ionic conductivity reported for a lithium aluminophosphate glass at room temperature (Table S1 in the SI).^{33,44–46}

3.4 Effect of annealing temperature

From Figure 1, the LAPO film composition with the highest σ_{ion} ($\text{Li}_{2.8}\text{Al}_1\text{P}_{1.25}\text{O}_x$) was chosen and the conductivity as a function of annealing temperature, T_{anneal} studied. An inverse relationship between σ_{ion} and T_{anneal} was discovered, with σ_{ion} decreasing by a factor of ≈ 4 from 230 to 400 °C (Figure 2). This observation is in contrast to the work of Clayton et al.,³³ who found negligible ionic conductivity ($\approx 10^{-10} \text{ S cm}^{-1}$) after annealing $\text{Li}_{2.5}\text{Al}_1\text{P}_{1.5}\text{O}_x$ films at 400 °C, suggesting a complex relationship between composition, annealing temperature and film structure.

The most conductive films had σ_{ion} values within an order of magnitude of state-of-the-art LiPON SEs ($\sigma_{\text{ion}} \approx 2 \times 10^{-6} \text{ S cm}^{-1}$).³⁴ We note that the LiPON SEs used in SSBs are typically several microns in thickness, so comparable bulk resistance values would be expected for the thinner LAPO films (i.e., 100's of nm) used here. Annealing at lower temperatures than 230 °C resulted in low quality films visually by eye. Crystallisation may occur at higher annealing temperatures and affect ionic properties. Laboratory GI-XRD showed no signal above the background of the fused silica substrates, indicating the films were non-crystalline at all annealing conditions investigated here (Figure S1 in the SI).

XPS was used to quantify the elemental composition and oxidation states of the films. Representative region scans can be located in Figure S2 in the SI. All films contained chemical species in the expected charge states: Li^+ , Al^{3+} , P^{5+}

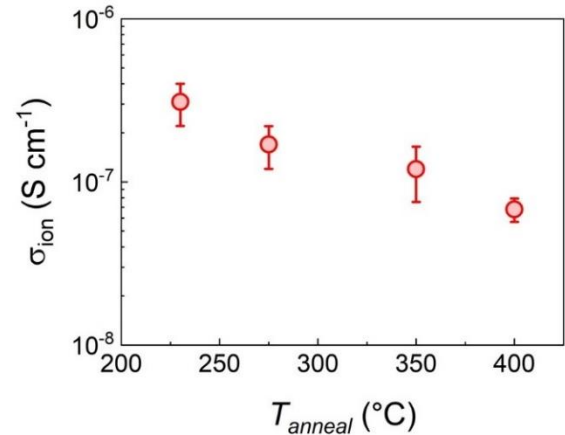


Figure 2. σ_{ion} variation for $\text{Li}_{2.8}\text{AlP}_{1.25}\text{O}_x$ films as a function of annealing temperature

and O^{2-} with a higher binding energy shoulder peak in the latter indicative of defective oxygen or surface hydroxides.^{47,48} No N signal was detected, consistent with the loss of nitrates during annealing. Table 1 contains the compositions of LAPO films annealed at different temperatures. At the intermediate T_{anneal} values of 275 and 350 °C, the measured values were in good agreement with

Table 1: Surface composition determined via XPS.

$T_{\text{anneal}} (^{\circ}\text{C})$	Stoichiometry in $\text{Li}_a\text{Al}_b\text{P}_c\text{O}_x$			
	a	b	c	x
230	3.0	1	1.4	5.2
275	2.8	1	1.3	5.1
350	2.7	1	1.3	5.2
400	2.9	1	1.2	5.6

stoichiometries expected based on the precursor solution composition. XPS is a surface sensitive technique, therefore this result implies chemical homogeneity throughout the film thickness. However, at the extremes of T_{anneal} , excess Li was measured, suggestive of chemical gradients in the films. At 400 $^{\circ}\text{C}$, the XPS results show greater Li and O

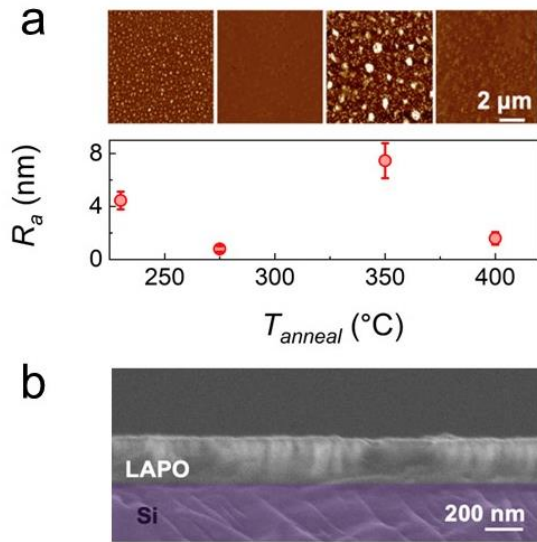


Figure 3. a) AFM of the surface of single layer films and their average roughness (R_a) as a function of annealing temperature displayed underneath. **b)** Cross-sectional SEM image of a 4-layer $\text{Li}_{2.8}\text{AlP}_{1.25}\text{O}_x$ film on an Si substrate annealed at 275 $^{\circ}\text{C}$.

contents at the film surface Li-O species would be expected to be ionically insulating and consistent with the lower σ_{ion} observed in Figure 2. On the other hand, at 230 $^{\circ}\text{C}$ greater relative Li and P concentrations were observed in addition to the highest σ_{ion} . Future work will investigate controlling the chemical inhomogeneity of the films during synthesis, e.g., by intentionally depositing layers of dissimilar composition, in addition to further exploration of the Li-Al-P-O phase space.

The film surface morphology as a function of annealing temperature was determined with AFM (Figure 3a). All films exhibited low average surface roughness (R_a) < 10 nm, with $T_{\text{anneal}} = 275$ $^{\circ}\text{C}$ exhibiting the lowest R_a of ≈ 1 nm. A complex relationship was evident and reproducible across multiple samples – likely due to competing processes such as evaporation and surface reorganisation during annealing.

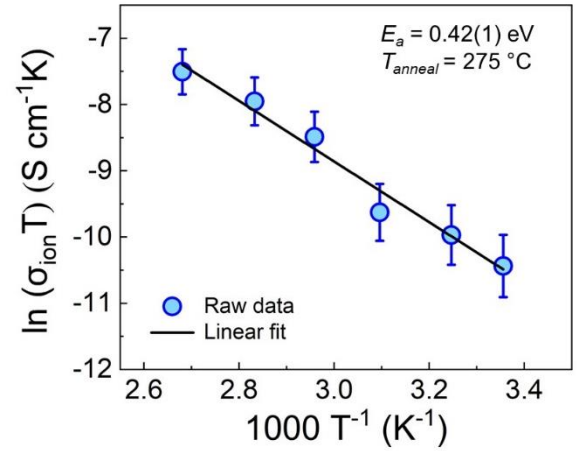


Figure 4: Temperature-dependent σ_{ion} measurements and activation energy analysis

The Young's modulus was determined by nanoindentation in the AFM to be 54(4) GPa. This value is greater than that of sulfide SEs (≈ 15 -20 GPa)^{16,49,50} and close to that of LiPON (77 GPa),¹⁵ suggestive of LAPO being sufficiently tough to suppress Li dendrite propagation. Due to the combination of low surface roughness, chemical homogeneity and near-peak ionic conductivity, 275 $^{\circ}\text{C}$ was chosen as the optimal annealing temperature for subsequent investigations – the abbreviation LAPO will refer to this film composition annealed under these conditions for the remainder of the manuscript. SEM imaging confirmed these SE films were continuous and dense (Figure 3b), with a single layer thickness of ≈ 75 nm.

3.5 Activation energy analysis

The activation energy, E_a of optimised LAPO was determined using an Arrhenius relationship (Equation 2, Figure 4) as 0.42(1) eV. This value is lower than those reported for thin film and bulk $\text{Li}_{2.5}\text{AlP}_{1.5}\text{O}_{5.5}$ glasses, 0.67 and ≈ 0.6 eV respectively,^{33,44} and even lower than that reported for LiPON (≈ 0.55 eV),¹⁵ despite the latter's higher room temperature conductivity. This can be rationalised by consid-

ering the greater Li content of LiPON⁵¹ compared to LAPO, which is incorporated in the conductivity pre-factor term in Equation 2. Additional differences in pre-factor parameters, e.g., hopping frequency, may also contribute. Returning to the other LAPO phases, additional Li in the structure could provide additional charge carriers. However, our optimised composition contains only slightly more Li ($\approx 10\%$) than those reported previously.

It is therefore likely that by altering the Li:Al:P ratios we have modified the glassy network of Al-O and P-O units, creating a more favourable pathways for Li⁺-ion transport. No significant differences were observed in XPS spectra and no structural information could be obtained by XRD (Figure S1 in the SI). Local structure studies using pair-distribution-function analysis and solid-state NMR techniques may help in better understanding these materials but are out of the scope of the present study.

3.6 Electronic conductivity

The bulk electronic conductivity (σ_e) of SEs has been suggested to be an important factor in the prevention of Li dendrites.¹⁴ To determine the σ_e , a DC voltage was applied, and the subsequent current decay monitored (Figure 5). From this steady-state current value, the σ_e of LAPO was calculated as $\approx 10^{-11}$ S cm⁻¹, ≈ 4 orders of magnitude lower than the σ_{ion} and yielding a transference number of ≈ 1 assuming only the Li⁺-ions are mobile. This value for LAPO compares well to that reported for LiPON ($\approx 10^{-11}$ - 10^{-14} S cm⁻¹),^{14,52} and is significantly lower than those for Li₇La₃Zr₂O₁₂ (LLZO) and Li₃PS₄ (LPS) SEs (Figure 5, inset).

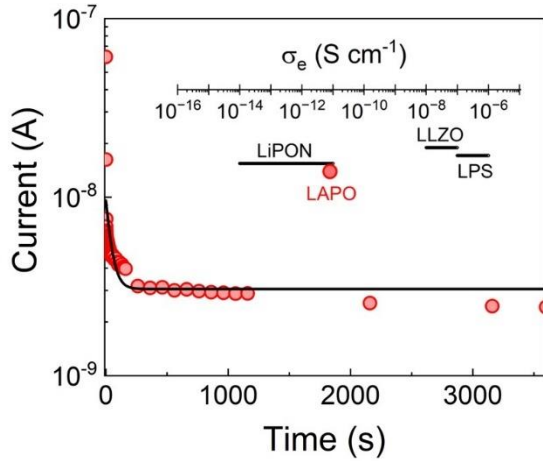


Figure 5: Current-voltage decay curve for a Li_{2.8}AlP_{1.25}O_x film annealed at 275 °C. Comparison of the σ_e of LAPO against SEs in literature (inset).

3.7 Stability against Li metal

The electrochemical stability of LAPO was tested against Li metal using time-resolved EIS (Figure 6a). The EIS data were fit using 3 $R|CPE$ units⁵³ (ECM inset in Figure 6a). Here, R_1 represented the bulk SE impedance (R_b), R_2 the

passivation layer (R_p) due to LAPO decomposition and R_3 the charge transfer at the Li interface. Distribution of relaxation times (DRT) analysis^{43,54} was used to deconvolute the different polarisation processes. To test the linearity, stability, and causality of the EIS data, the Kramers-Kroning relation was first applied.³⁹ The residuals were fixed to be $\pm 1\%$ for the processes occurring at high-to-mid frequencies corresponding to the passivation and bulk SE resistances R_b and R_p , respectively. However, at mid-to-low frequencies the DRT residuals were outside the set range, possibly due to the non-linear nature of the charge transfer reactions occurring at the Li interface. Therefore, it was

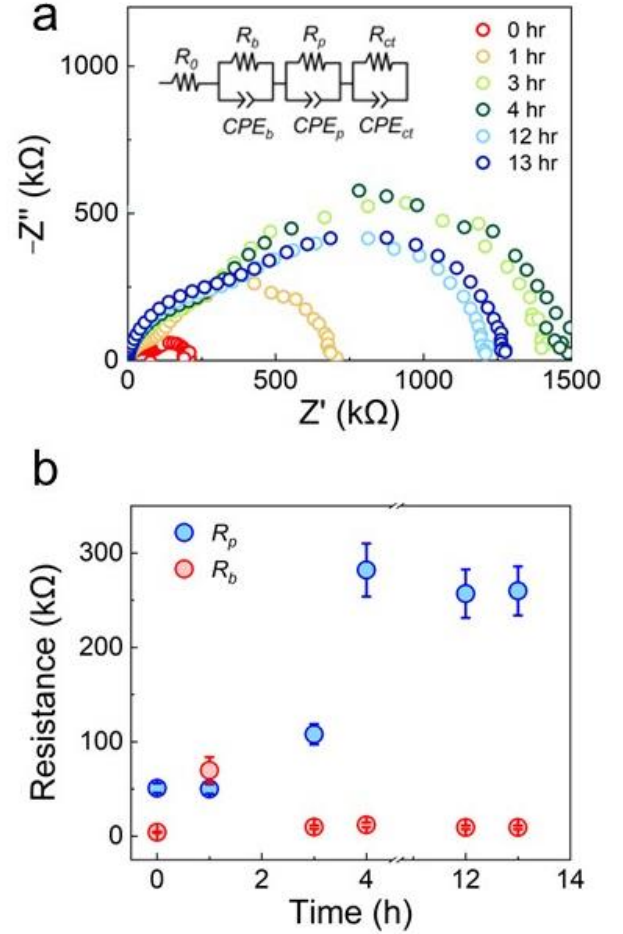


Figure 6: **a)** EIS Nyquist spectra of Li_{2.8}AlP_{1.25}O_x against Li metal over 13 hrs. **b)** Comparison of R_b and R_p vs. time. The resistance values were extracted from DRT analysis (Figure S3 in the SI).

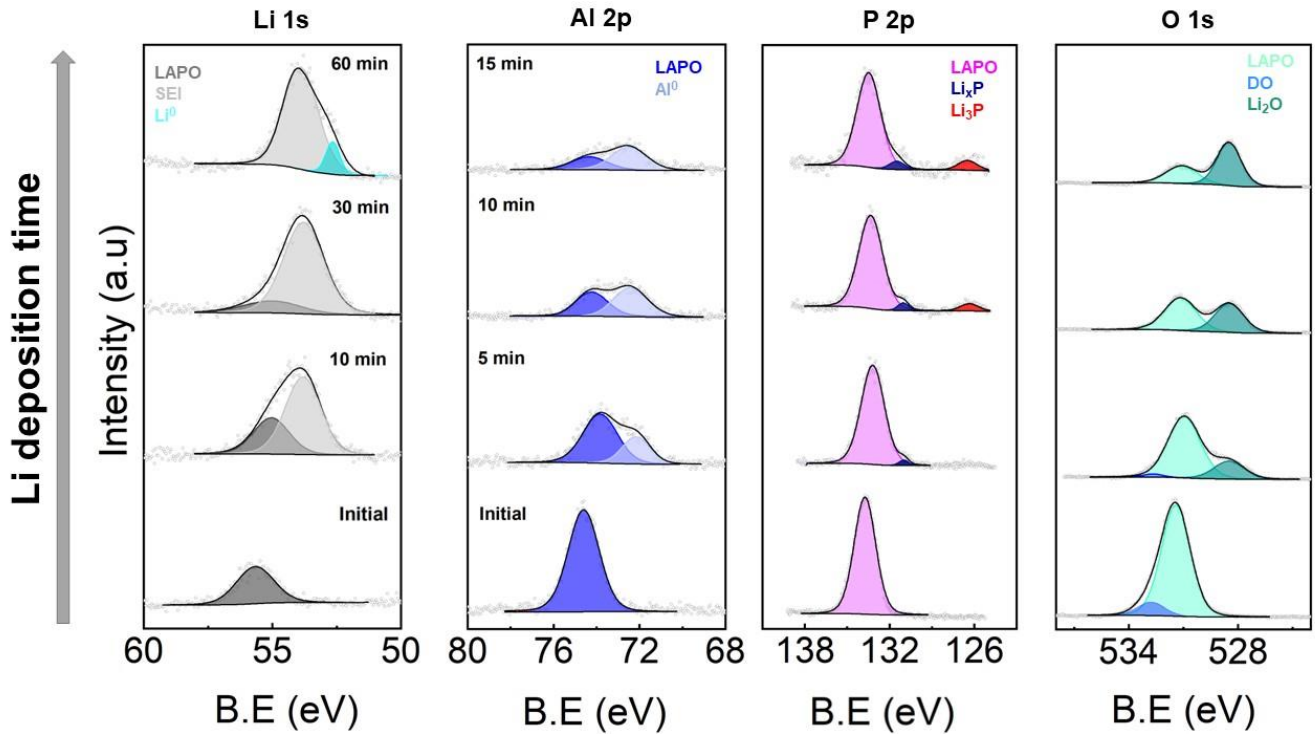


Figure 7: Evolution of core level XPS spectra during Li deposition on the $\text{Li}_{2.8}\text{AlP}_{1.25}\text{O}_x$ surface. Note that the deposition times given for the Al 2p spectra also apply for P 2p and O 1s panels.

not possible to meaningfully quantify the R_{ct} values. The non-linearity of the R_{ct} and shift in time processes can be observed in the DRT plot (Figure S3 in the SI). Figure 6b shows that R_b was fairly invariant with time, with an anomaly at 1 h which we attribute to the unstable decomposition reaction of LAPO with Li. A stable passivation layer or interphase was formed after ≈ 4 hours with a $\approx 25\times$ greater impedance than the bulk SE.

3.8 In situ XPS during Li deposition

To elucidate the interphase composition, we performed in situ XPS, monitoring the core-level photoemission spectra Li 1s, Al 2p, P 2p and O 1s during Li deposition (Figure 7). In all cases, the pristine components remained in addition to new features caused by reaction with Li, suggesting either that LAPO exists as part of the passivation layer or that this layer is thin enough to permit sampling of the underlying SE. In the case of Li 1s, a new feature appeared at lower BE (≈ 53.7 eV). This was likely due to the formation of Li-containing decomposition products, such as Li_2O , Li_3P , Li_xP and surface-absorbed contaminants such as Li_2CO_3 , etc. After 60 min, an additional peak at lower BE emerged (≈ 52.7 eV) associated with Li^0 . A significant fraction of the Al^{3+} initially present was reduced to Al^0 during Li deposition, whilst P^{5+} was reduced to Li_3P (126.5 eV) and partially reduced Li_xP species (131.0 eV). A very similar evolution of the P 2p spectra was observed during in

situ XPS of LiPON⁵⁵. Finally, a new feature at lower BE was detected in the O 1s spectra, which grew to dominate with time and could be assigned to Li_2O . Although there will be some Li_2O present due to the deposited Li reacting with surface contaminants and trace $\text{O}_2/\text{H}_2\text{O}$ present inside the XPS chamber,⁵⁶ it is likely that a majority of the Li_2O formed as a result of direct reaction with LAPO considering the greater impedance of the interphase. Therefore, the passivation layer was found to be a mixture of Li_2O , Li_3P , Li_xP and Al^0 species. A stable interphase should contain ionically conducting and electronically insulating decomposition products.⁵⁷ Considering the chemical information from XPS and the resistive interphase revealed by EIS, we speculate that the electrically conductive components (Li_xP , Al^0) were isolated in a matrix of Li_2O and Li_3P which are known electronic insulators.⁵⁸

4. CONCLUSIONS

In summary, we synthesised non-crystalline Li^+ -ion SE thin films from aqueous solutions. Through systematic exploration of the Li-Al-P-O phase space, an optimal composition of $\text{Li}_{2.8}\text{AlP}_{1.25}\text{O}_x$ was identified with an $\sigma_{\text{ion}} > 10^{-7} \text{ S cm}^{-1}$ at room temperature. Both increased Li and decreased P content were required to maximise the ionic conductivity. Higher annealing temperatures led to decreased σ_{ion} between 230 and 400 °C in this system, despite remaining X-

ray amorphous at all temperatures studied. XPS hinted that annealing may induce chemical gradients in the films. Film surface roughness exhibited a complex dependence on annealing temperature, with the smoothest films being produced at 275 °C. Temperature-dependent σ_{ion} measurements yielded a low activation energy of 0.42(1) eV, indicating facile Li⁺-ion transport in this non-crystalline SE. DC polarisation experiments revealed a low σ_e ($\approx 10^{-11}$ S cm⁻¹) and a moderate Young's modulus of ≈ 54 GPa was also determined. In contact with Li metal, LAPO formed a stable, but resistive passivation layer and in situ XPS showed this to consist of Li₂O, Li₃P, Li_xP and Al⁰ species. Our findings should motivate future investigations into solution-processed non-crystalline SEs and have established a foundation to further improve their bulk and interfacial properties for use in advanced energy storage devices.

AUTHOR INFORMATION

Corresponding Author

* For correspondence: a.rettie@ucl.ac.uk

Author Contributions

The manuscript was written through contributions of all authors. All authors have given approval to the final version of the manuscript.

Notes

PV, AR and TG have applied for a provisional patent relating to this work.

ACKNOWLEDGMENT

We gratefully acknowledge the EPSRC (EP/W029235/1 and DTP Studentships for PV and TG: EP/R513143/1, EP/T517793/1), the Faraday Institution LiSTAR programme (FIRG014, EP/S003053/1) and UCL for start-up funding.

REFERENCES

- 1 C. Xu, Q. Dai, L. Gaines, M. Hu, A. Tukker and B. Steubing, *Commun. Mater.* 2020, **1**, 1-10.
- 2 W. Chen, J. Liang, Z. Yang and G. Li, *Energy Procedia*, 2019, **158**, 4363–4368.
- 3 P. Albertus, S. Babinec, S. Litzelman and A. Newman, *Nat. Energy*, 2018, **3**, 16-21.
- 4 J. Janek and W. G. Zeier, *Nat. Energy*, 2016, **1**, 16141.
- 5 M. D. Tikekar, S. Choudhury, Z. Tu and L. A. Archer, *Nat. Energy*, 2016, **1**, 1–7.
- 6 P. G. Bruce, S. A. Freunberger, L. J. Hardwick and J.-M. Tarascon, *Nat. Mater.*, 2012, **11**, 19–29.
- 7 N. Kamaya, K. Homma, Y. Yamakawa, M. Hirayama, R. Kanno, M. Yonemura, T. Kamiyama, Y. Kato, S. Hama, K. Kawamoto and A. Mitsui, *Nat. Mater.*, 2011, **10**, 682–686.
- 8 T. Nakamura, K. Amezawa, J. Kulisch, W. G. Zeier and J. Janek, *ACS Appl. Mater. Interfaces*, 2019, **11**, 19968–19976.
- 9 A. Manthiram, X. Yu and S. Wang, *Nat. Rev. Mater.*, 2017, **2**, 16103.
- 10 R. C. Xu, X. H. Xia, S. Z. Zhang, D. Xie, X. L. Wang and J. P. Tu, *Electrochim. Acta*, 2018, **284**, 177–187.
- 11 Z. A. Grady, C. J. Wilkinson, C. A. Randall and J. C. Mauro, *Front. Energy Res.*, 2020, **8**, 1–23.
- 12 M. Balaish, J. C. Gonzalez-Rosillo, K. J. Kim, Y. Zhu, Z. D. Hood and J. L. M. Rupp, *Nat. Energy*, 2021, **6**, 227–239.
- 13 J. Sastre, M. H. Futscher, L. Pompizi, A. Aribia, A. Priebe, J. Overbeck, M. Stiefel, A. N. Tiwari and Y. E. Romanyuk, *Commun. Mater.* 2021, **2**, 1-10.
- 14 F. Han, A. S. Westover, J. Yue, X. Fan, F. Wang, M. Chi, D. N. Leonard, N. J. Dudney, H. Wang and C. Wang, *Nat. Energy*, 2019, **4**, 187–196.
- 15 V. Lacivita, N. Artrith and G. Ceder, *Chem. Mater.*, 2018, **30**, 7077–7090.
- 16 A. Kato, M. Nagao, A. Sakuda, A. Hayashi and M. Tatsumisago, *J. Ceram. Soc. Japan*, 2014, **122**, 552–555.
- 17 J. B. Bates, N. J. Dudney, B. Neudecker, A. Ueda and C. D. Evans, *Solid State Ionics*, 2000, **135**, 33–45.
- 18 A. S. Westover, N. J. Dudney, R. L. Sacci and S. Kalnaus, *ACS Energy Lett.*, 2019, **4**, 651–655.
- 19 P. Albertus, V. Anandan, C. Ban, N. Balsara, I. Belharouak, J. Buettner-Garrett, Z. Chen, C. Daniel, M. Doeff, N. J. Dudney, B. Dunn, S. J. Harris, S. Herle, E. Herbert, S. Kalnaus, J. A. Libera, D. Lu, S. Martin, B. D. McCloskey, M. T. McDowell, Y. S. Meng, J. Nanda, J. Sakamoto, E. C. Self, S. Tepavcevic, E. Wachsman, C. Wang, A. S. Westover, J. Xiao and T. Yersak, *ACS Energy Lett.*, 2021, **6**, 1399–1404.
- 20 S. Kalnaus, A. S. Westover, M. Kornbluth, E. Herbert and N. J. Dudney, *J. Mater. Res.*, 2021, **36**, 787–796.
- 21 D. Cheng, T. A. Wynn, X. Wang, S. Wang, M. Zhang, R. Shimizu, S. Bai, H. Nguyen, C. Fang, M. cheol Kim, W. Li, B. Lu, S. J. Kim and Y. S. Meng, *Joule*, 2020, **4**, 2484–2500.
- 22 A. S. Westover, R. L. Sacci and N. Dudney, *ACS Energy Lett.*, 2020, **5**, 3860–3867.
- 23 W. Liu, R. Guo, B. Zhan, B. Shi, Y. Li, H. Pei, Y. Wang, W. Shi, Z. Fu and J. Xie, *ACS Appl. Energy Mater.*, 2018, **1**, 1674–1679.

- 24 H. Zhou, S. Yu, H. Liu and P. Liu, *J. Power Sources*, 2020, **450**, 227632.
- 25 W. Wang, X. Yue, J. Meng, J. Wang, X. Wang, H. Chen, D. Shi, J. Fu, Y. Zhou, J. Chen and Z. Fu, *Energy Storage Mater.*, 2019, **18**, 414–422.
- 26 T. Krauskopf, F. H. Richter, W. G. Zeier and J. Janek, *Chem. Rev.*, 2020, **120**, 7745–7794.
- 27 J. Schnell, H. Knörzer, A. J. Imbsweiler and G. Reinhart, *Energy Technol.*, 2020, **8**, 1901237.
- 28 A. Chen, C. Qu, Y. Shi and F. Shi, *Front. Energy Res.*, 2020, **8**, 226.
- 29 T. T. Bui, B. Yun, K. Darko, S. B. Shin, J. Kim, J. Hong, M. Lee, S. K. Park and M.-G. Kim, *Adv. Mater. Interfaces*, 2021, **8**, 2001767.
- 30 R. J. Chen, M. Huang, W. Z. Huang, Y. Shen, Y. H. Lin and C. W. Nan, *J. Mater. Chem. A*, 2014, **2**, 13277–13282.
- 31 Z. Zheng, H. Fang, F. Yang, Z.-K. Liu and Y. Wang, *J. Electrochem. Soc.*, 2014, **161**, A473–A479.
- 32 S. T. Meyers, J. T. Anderson, D. Hong, C. M. Hung, J. F. Wager and D. A. Keszler, *Chem. Mater.*, 2007, **19**, 4023–4029.
- 33 D. R. Clayton, D. Lepage, P. N. Plassmeyer, C. J. Page and M. C. Lonergan, *RSC Adv.*, 2017, **7**, 7046–7051.
- 34 J. B. Bates, N. J. Dudney, G. R. Gruzalski, R. A. Zuhr, A. Choudhury, C. F. Luck and J. D. Robertson, *Solid State Ionics*, 1992, **53–56**, 647–654.
- 35 B. V. Derjaguin, V. M. Muller and Y. P. Toporov, *J. Colloid Interface Sci.*, 1975, **53**, 314–326.
- 36 S. Wenzel, S. J. Sedlmaier, C. Dietrich, W. G. Zeier and J. Janek, *Solid State Ionics*, 2018, **318**, 102–112.
- 37 A. Lasia, *Electrochem. Impedance Spectrosc. its Appl.*, 2014, **9781461489**, 1–367.
- 38 U. Westerhoff, K. Kurbach, F. Lienesch and M. Kurrat, *Energy Technol.*, 2016, **4**, 1620–1630.
- 39 P. Vadhva, J. Hu, M. J. Johnson, R. Stocker, M. Braglia, D. J. L. Brett and A. J. E. Rettie, *ChemElectroChem*, 2021, **8**, 1930–1947.
- 40 Y. Gao, A. M. Nolan, P. Du, Y. Wu, C. Yang, Q. Chen, Y. Mo and S. H. Bo, *Chem. Rev.*, 2020, **120**, 5954–6008.
- 41 N. S. C. Priya, K. Sandhya and D. N. Rajendran, *Electrochem. Energy Technol.*, 2018, **3**, 49–53.
- 42 M. C. Pang, Y. Hao, M. Marinescu, H. Wang, M. Chen and G. J. Offer, *Phys. Chem. Chem. Phys.*, 2019, **21**, 22740–22755.
- 43 T. H. Wan, M. Saccoccio, C. Chen and F. Ciucci, *Electrochim. Acta*, 2015, **184**, 483–499.
- 44 C. V. K. Reddy, R. B. Rao, K. C. Mouli, D. V. R. Koti Reddy and M. V. R. Reddy, *J. Mater. Sci.*, 2012, **47**, 6254–6262.
- 45 M. V. N. V. D. Sharma, A. V. Sarma and R. Balaji Rao, *J. Mater. Sci.*, 2009, **44**, 5557–5562.
- 46 F. Moreau, A. Durán and F. Muñoz, *J. Eur. Ceram. Soc.*, 2009, **29**, 1895–1902.
- 47 M. C. Biesinger, L. W. M. Lau, A. R. Gerson and R. S. C. Smart, *Appl. Surf. Sci.*, 2010, **257**, 887–898.
- 48 M. C. Biesinger, B. P. Payne, A. P. Grosvenor, L. W. M. Lau, A. R. Gerson and R. S. C. Smart, *Appl. Surf. Sci.*, 2011, **257**, 2717–2730.
- 49 A. Hayashi, A. Sakuda and M. Tatsumisago, *Front. Energy Res.*, 2016, **4**, 25.
- 50 X. Ke, Y. Wang, G. Ren and C. Yuan, *Energy Storage Mater.*, 2020, **26**, 313–324.
- 51 B. Fleutot, B. Pecquenard, H. Martinez, M. Letellier and A. Levasseur, *Solid State Ionics*, 2011, **186**, 29–36.
- 52 L. Le Van-Jodin, F. Ducroquet, F. Sabary and I. Chevalier, *Solid State Ionics*, 2013, **253**, 151–156.
- 53 L. M. Riegger, R. Schlem, J. Sann, W. G. Zeier and J. Janek, *Angew. Chemie - Int. Ed.*, 2021, **60**, 6718–6723.
- 54 T. H. Wan and F. Ciucci, *Electrochim. Acta*, 2020, **331**, 135355.
- 55 A. Schwöbel, R. Hausbrand and W. Jaegermann, *Solid State Ionics*, 2015, **273**, 51–54.
- 56 J. S. Gibson, S. Narayanan, J. E. N. Swallow, P. Kumar-Thakur, M. Pasta, T.-L. Lee and R. S. Weatherup, *Faraday Discuss.*, 2022, **236**, 267–287.
- 57 S. Wenzel, T. Leichtweiss, D. Krüger, J. Sann and J. Janek, *Solid State Ionics*, 2015, **278**, 98–105.
- 58 L. Yuheng, C. Pieremanuele and G. Prashun, *PRX Energy*, 2022, **1**, 023004.

ASSOCIATED CONTENT

Supporting Information. Ionic conductivity comparison, XRD additional XPS and DRT analyses are provided.

